RESEARCH PAPER



A maximum-rectifier-function approach to stress-constrained topology optimization

Julián A. Norato¹ · Hollis A. Smith¹ · Joshua D. Deaton² · Raymond M. Kolonay²

Received: 25 February 2022 / Revised: 17 July 2022 / Accepted: 1 August 2022 © The Author(s), under exclusive licence to Springer-Verlag GmbH Germany, part of Springer Nature 2022

Abstract

This paper introduces a novel method for stress-constrained topology optimization in which the stress constraint is a differentiable approximation of the maximum element stress violation in the structure. The element stress violation is given by a differentiable rectifier function. A key feature of the proposed method is its ability to render designs that satisfy the stress limit without renormalization of the constraint, as in some existing aggregation approaches. Numerical experiments demonstrate that the proposed technique exhibits better convergence and is less sensitive to the aggregation parameter than aggregation methods that employ renormalization. The effectiveness of the proposed method is demonstrated by several examples.

Keywords Stress constraints · Aggregation functions · Constraint scaling

1 Introduction

The incorporation of stress constraints in topology optimization is of paramount importance, since multiple structural design criteria driven by material failure are formulated in terms of stress. This importance is reflected in the volume of publications on this topic, which, at the time of writing this manuscript, is in the thousands. The design problem typically consists of minimizing the structural weight subject to

Responsible Editor: Josephine Voigt Carstensen

In memoriam of Pauli Pedersen (1937–2021)
Preliminary results of this work were presented at the 14th World
Congress in Structural and Multidisciplinary Optimization in
2021.

Distribution Statement A: Approved for Public Release; Distribution is Unlimited. PA# AFRL-2022-3456. Topical Collection: 14th World Congress of Structural and Multidisciplinary Optimization. Guest Editors: Y. Noh, E. Acar, J. Carstensen, J. Guest, J. Norato, and P. Ramu.

Published online: 21 September 2022

- Department of Mechanical Engineering, University of Connecticut, 191 Auditorium Road, U-3139, Storrs, CT 06269, USA
- Multidisciplinary Science and Technology Center, Air Force Research Lab, Wright-Patterson Air Force Base, Dayton, OH 45433, USA

a constraint that the stress anywhere in the structure does not exceed a specified value. One of the challenges presented by this problem is the local nature of stress and thus of the constraint. If the stress limit must be satisfied at, for example, every element centroid, then there are as many constraints as elements in the finite element mesh. The ensuing large number of constraints necessitates an equally large number of adjoint analyses to compute design sensitivities (cf. Duysinx and Bendsøe 1998), which makes the computational cost for practical problems prohibitive.

As detailed in the recent comparative study by da Silva et al. (2021), there are two strategies to address this challenge. The first approach is to recast the local constraints as a single constraint that the maximum stress in the structure does not exceed the prescribed limit (or that the maximum element stress violation does not exceed zero). Techniques in this category are often called aggregation approaches [for example, Kennedy and Hicken (2015)]. Since the maximum function is not differentiable, smooth approximations are employed (Yang and Chen 1996; Duysinx and Sigmund 1998) so that efficient gradient-based methods can be used for the optimization. These approximations include, for example, the *P*-norm, *P*-mean, and the Kreisselmeier–Steinhauser (KS) function (cf. Verbart et al. 2017).

The second strategy consists of adding the constraints to the objective function, either as an exterior penalty (e.g., Amstutz and Novotny 2010; De Troya and Tortorelli 2018) or through an augmented Lagrangian (AL) approach (cf.



Pereira et al. 2004; Senhora et al. 2020; Giraldo-Londoño et al. 2021). The constraints are multiplied by a parameter (a penalty or Lagrange multiplier estimate) and the optimization is solved as a sequence of problems with increasing values of the parameter. Although these approaches do not use approximations of the maximum, they share the common characteristic that adding all the local constraints as terms to the objective function requires only one adjoint analysis per load case to compute design sensitivities. Herein, we collectively refer to these techniques as penalty methods.

A particular challenge of aggregation methods is that the approximations of the maximum stress may significantly overshoot or undershoot the true maximum. Consequently, the optimization renders a design that is conservative or unsafe, respectively. Increasing the parameter of the approximation will increase the accuracy, as these approximations tend to the true maximum in the limit when the parameter tends to infinity. However, this also causes the constraint to be more nonlinear, which consequently hinders the optimization. This happens because in this case approximations of the constraint are reasonably accurate only within a very small neighborhood of the current design. In practice, this means the optimizer may take poor steps, leading to a large number of iterations to converge or causing the iterative process to altogether diverge. A solution to this problem was introduced by Le et al. (2010), whereby the limit of the constraint is adaptively rescaled throughout the optimization based on the values of the true and approximate maximum stresses of the current design. The idea is to increase, decrease, or leave unchanged the constraint limit if the true maximum stress is below, exceeds, or equals the desired stress limit, respectively. We interchangeably refer to this heuristic technique as adaptive constraint scaling (ACS) or renormalization. This method is highly effective in tightly satisfying the specified stress limit.

Penalty approaches do not require renormalization to satisfy the stress limit and they are backed by proofs that they converge to a local minimum of the original optimization problem. Moreover, the local constraints added to the objective function need not be differentiable everywhere; for instance, the penalty term for each local constraint may correspond to the true maximum between zero and the element violation. They require, however, a strategy to initialize and update the penalty parameters. The performance of these methods can be highly sensitive to this initialization and updating strategy, with poor choices of the penalty parameters potentially leading to negligible or no improvement in early iterations or to divergence from a good initial design (Birgin et al. 2005; Curtis et al. 2016), particularly for the exterior penalty methods. Methods that use the AL approach have nevertheless reported a robust behavior with a problem-independent parameter updating strategy (Senhora et al. 2020). Another consideration in penalty approaches is the incorporation of multiple constraints in the augmented Lagrangian, in which different parameters may have to be chosen for different constraints, see the discussion in Russ and Waisman (2021).

An additional challenge of the aggregation approaches is that the value of the parameter for the approximated maximum function needed to produce good results can be highly mesh dependent, as noted in Zhou and Sigmund (2017). Furthermore, the convergence behavior when using renormalization can be quite noisy, and the optimization can render suboptimal designs.

In this work, we present a method to incorporate stress criteria in the topology optimization in which the local stress constraints are cast into a single, separate constraint as in aggregation methods, but without constraint renormalization. The stress constraint in the proposed method consists of a differentiable approximation of the maximum elementstress violation; in turn, the local constraint is given by a differentiable rectifier function, i.e., the maximum between zero and the element-stress violation (scaled by the stress limit). We use the term rectifier following the terminology for this type of function used in the field of artificial neural networks. Since a key goal of our method is to circumvent the need for renormalization in aggregation methods, particular emphasis is given to comparing the proposed approach with an aggregation method that uses renormalization, namely the technique of Le et al. (2010).

We note that other works have used rectifier functions in stress-constrained topology optimization. For example, the penalty approaches of Amstutz and Novotny (2010) and De Troya and Tortorelli (2018) use a smooth approximation of the ramp function based on the P-norm. The aggregation approach of Wang and Qian (2018) uses a smooth Heaviside approximation based on the arctan function and employs renormalization. The technique of Zhang et al. (2020) uses an exponential smooth hinge function as rectifier, and the aggregate stress constraint requires that the average rectifier does not exceed a small value; this method does not use renormalization, and the authors report that the stress limit is not tightly satisfied. The approach that is perhaps closest in spirit to the one proposed in this work is in fact one of the earliest works in stress-constrained topology optimization, namely the method of Duysinx and Sigmund (1998). In that work, a P-norm of a rectifier function is used as the stress constraint; the rectifier is the (true) maximum between zero and a function that is based on the element stress constraint violation, but that also incorporates additional terms to address the singular optimum problem (see Sect. 2.1) based on ε -relaxation. This approach predates renormalization techniques and, as reported by the authors, does not render a tight stress limit satisfaction.

The rest of the paper is structured as follows. Section 2 details the formulation of the proposed method maximum



rectifier function (MRF) method; it also recasts the ACS approach using a consistent notation that allows for a sensitivity analysis formulation that accommodates both approaches. Numerical examples in 2D and 3D to compare the two approaches are subsequently presented in Sect. 3, and we draw conclusions of this work in Sect. 4.

2 Formulation

This section details the formulation of the proposed stress-constrained topology optimization. We start by defining the element relaxed von Mises stress, which is the local quantity we constrain in the optimization. Next, we define the rectifier function that smoothly approximates the constraint violation at each element. We then define the aggregation function that captures the maximum constraint violation in the structure. Finally, we state the optimization problem with the proposed constraint.

2.1 Relaxed stress

As in all density-based methods, we consider element uniform pseudo-densities $\rho_{\rm e}$ as the design variables in the optimization. A linear filter of these variables is employed to enforce a minimum length scale and to render mesh-independent solutions. The vector of element filtered densities is given by

$$\bar{\rho} := \mathbf{H} \rho$$

$$H_{ij} := \frac{w_i^e \rho_i}{\sum_{i=1}^{n_e} w_i^e \rho_i}$$

$$w_i^e := \max\left(0, 1 - \frac{\|\mathbf{x}_e - \mathbf{x}_i\|}{r}\right),$$
(1)

with r the filter radius, $n_{\rm e}$ the number of elements, and ρ the vector of design variables. \mathbf{x}_i denotes the centroid of element i. Matrix \mathbf{H} is computed once at the beginning of the optimization. We note this corresponds to the consistent filtering approach (Bruns and Tortorelli 2001; Bourdin 2001), in which design variables are filtered and consistent sensitivities are subsequently computed.

Using the filtered density, an ersatz material is defined for element e with constitutive elasticity tensor

$$\mathbb{C}_{\mathbf{e}} := \hat{\rho}_{\mathbf{e}} \mathbb{C}_0 \tag{2}$$

$$\hat{\rho}_{e}(\bar{\rho}_{e};p) := (\rho_{\min} + (1 - \rho_{\min})\bar{\rho}_{e}^{p}), \tag{3}$$

where \mathbb{C}_0 is the elasticity tensor of the solid material, p is a penalization power, and $0 < \rho_{\min} \ll 1$ is a small bound to prevent an ill-posed analysis. This form of material interpolation corresponds to the modified solid isotropic material

interpolation (SIMP) scheme (Bendsøe and Sigmund 1999; Sigmund 2007), while the standard SIMP interpolation corresponds to $\rho_{\min} = 0$. The modified SIMP scheme has the advantage that the minimum material stiffness is independent of p, and, crucially, it allows for the element densities $\rho_{\rm e}$ to be zero, which is advantageous for the stress-constrained problem, as discussed later in this section.

Without loss of generality, and as is common in stress-constrained topology optimization, we consider the stress at the element centroid \mathbf{x}_e . The finite element (FE) analysis of the structure is carried out using the interpolated properties of (2) for each element, and the corresponding FE stress (in vector Voigt notation) is computed as

$$\sigma_{e} = \mathbb{C}_{e} \mathbf{B}_{e} \mathbf{u}_{e}, \tag{4}$$

where \mathbf{B}_{e} is the matrix corresponding to the symmetric gradient of the shape functions evaluated at \mathbf{x}_{e} , and \mathbf{u}_{e} is the element vector of nodal displacements.

The stress invariant we choose to constrain is the von Mises stress. The FE von Mises stress is given by

$$\sigma_{v_{\rm e}} = \sqrt{\sigma_{\rm e}^{\rm T} \mathbf{V} \sigma_{\rm e}},\tag{5}$$

where **V** is the $3(n-1) \times 3(n-1)$ matrix with components

$$V_{ij} = \begin{cases} 1 & \text{if } i = j \text{ and } i, j \le n \\ -\frac{1}{2} & \text{if } i \ne j \text{ and } i, j \le n \\ 3 & \text{if } i = j \text{ and } i, j > n \\ 0 & \text{otherwise,} \end{cases}$$
 (6)

for problems in \mathbb{R}^n and $n \in \{2, 3\}$. From (2), (3) and (5), it follows that

$$\sigma_{v_{\rm e}} = \hat{\rho}_{\rm e} s_{\rm e} \tag{7}$$

$$s_{e} := \sqrt{\sigma_{e_0}^{\mathsf{T}} \mathbf{V} \sigma_{e_0}} \tag{8}$$

$$\boldsymbol{\sigma}_{e_0} := \mathbb{C}_0 \mathbf{B}_{\mathbf{e}} \mathbf{u}_{\mathbf{e}}. \tag{9}$$

The reader is referred to "Appendix" for a discussion on robustly calculating σ_{ν_a} in the computer implementation.

As per the discussion in Le et al. (2010), we cannot use the FE stress of (5) in the constraint as the optimizer will render the trivial solution $\rho_e = 0 \,\forall e$. To see why this occurs, consider a homogeneous design for which $\rho_e = \rho^*$. Correspondingly, $\bar{\rho}_e = \rho^*$ and $\hat{\rho}_e = \rho_{\min} + (1 - \rho_{\min})\rho^{*p} = : \hat{\rho}_e^*$ from (1) and (3), respectively, and the element elasticity tensor from (2) is $\mathbb{C}_e = \hat{\rho}_e^* \mathbb{C}_0$. Consequently, the linearity of the analysis dictates that $\mathbf{u}_e = (1/\hat{\rho}_e^*)\mathbf{u}_{e_s}$, where \mathbf{u}_{e_s} denotes the displacement that would be obtained if the entire structure were fully solid. From (8) and (9), we then



have $s_{\rm e}=(1/\hat{\rho}_{\rm e}^*)s_{\rm e_s}$, where $s_{\rm e_s}$ is the von Mises stress corresponding to the fully-solid structure. Substituting in (7), we find that $\sigma_{v_{\rm e}}=s_{\rm e_s}$, that is, the finite element stress for a homogeneous design is independent of the value of ρ^* and therefore removing material will not affect the stress. If $s_{\rm e_s}$ does not exceed the specified stress limit for any element, the trivial design is therefore the optimal minimum-mass design.

The quantity s_e in (8) cannot be used as an element constraint either. Due to static indeterminacy, reducing ρ_e —which will make the element material more compliant by (2)—may decrease the amount of load going through the element, thus decreasing the strain $\mathbf{B}_e\mathbf{u}_e$ in (9) and consequently s_e . However, unless the element is in pure rigid-body motion, its strain will in general be non-zero even if $\rho_e = 0$ (for which $\hat{\rho}_e = \rho_{\min}$). If s_e exceeds the specified stress limit for some intermediate value of ρ_e , the optimizer will be unable to further decrease ρ_e , which has the effect of making it difficult to remove gray regions from the design. More importantly, a better design may be obtained altogether by removing the element from the analysis, in which case there simply is no constraint associated with that element.

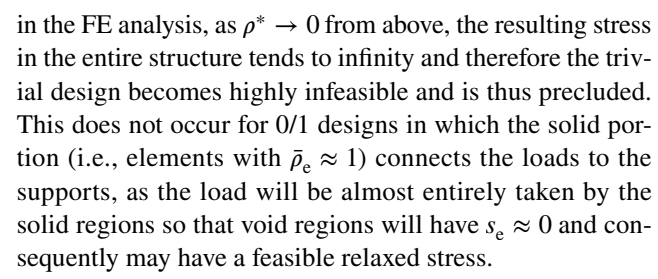
The foregoing phenomenon is the so-called singular optimum problem (Kirsch 1990; Cheng and Jiang 1992; Rozvany and Birker 1994), in which the global optimum lies in a degenerate (lower dimensional) region of the design space that cannot be reached by gradient-based optimizers. This region corresponds to one or more of the design variables being zero and their corresponding element constraints removed. The two primary strategies to circumvent this issue are the ε -relaxation technique (Cheng and Guo 1997; Rozvany and Sobieszczanski-Sobieski 1992; Duysinx and Bendsøe 1998; Duysinx and Sigmund 1998) and the qp approach of Bruggi (2008) [also used in Le et al. (2010)]. Herein we employ the latter and define a relaxed stress

$$\tilde{\sigma}_{v_e} := \tilde{\rho}_e s_e \tag{10}$$

$$\tilde{\rho}_{e} := \bar{\rho}_{e}^{p-q},\tag{11}$$

where q is a relaxation power that must satisfy $0 . Using the relaxed stress of (10) instead of the FE stress of (4) to define the stress constraint has the effect of opening up the degenerate regions in the design space so that they can be reached by the optimizer. Alternatively, (10) can be seen as a penalization where intermediate densities render a lower strength-to-volume ratio than fully-solid material and lead to an infeasible design. A consequence of this stress relaxation is that when <math>\bar{\rho}_e = 0$, the corresponding element stress constraint is effectively removed from the optimization.

Following the same argument as before, for a homogeneous design with $\rho_e = \rho^*$, the relaxed stress of (10) is $\tilde{\sigma}_{v_e} = (\rho_e^*)^{p-q-1} s_{e_s}$. Since p-q-1<0 and s_{e_s} are bounded



A subtle but important point must be made about the definition of (11). As per the previous discussion, a requirement of the relaxation is that $\lim_{\bar{\rho}_c \to 0, s_e \to 0} \tilde{\sigma}_{v_e} = 0$. Therefore, we cannot use $\tilde{\rho}_e = \hat{\rho}_e(\bar{\rho}_e;p)/\bar{\rho}_e^q$, because $\hat{\rho}_e$ is bounded below by ρ_{\min} , hence the limit would be infinity. An alternative definition is $\tilde{\rho}_e = \hat{\rho}_e(\bar{\rho}_e;p)/\hat{\rho}_e(\bar{\rho}_e;q)$, for which $\tilde{\rho}_e = 1$ when $\bar{\rho}_e = \rho_{\min}$ and thus $\lim_{\bar{\rho}_e \to 0} \tilde{\sigma}_{v_e} = s_e$, which leads again to the singular optima phenomenon previously discussed. The expression of (11), on the other hand, tends exactly to zero in the limit, and this is the advantage of using the modified SIMP interpolation. The combined use of (2) for the material interpolation and (11) for the stress relaxation has been employed by other works [for example, by Oest and Lund (2017) and Zhang et al. (2019) for fatigue-constrained topology optimization].

2.2 Local stress constraint

In the proposed approach, the local constraint is a rectifier of the element stress constraint violation. Multiple loading cases can be applied to the structure, each with a possibly different stress limit. The element stress constraint for loading case k is given by

$$h(\tilde{\sigma}_{v_e k}) := \max\left(0, \frac{\tilde{\sigma}_{v_e k}}{\sigma_k^*} - 1\right) \le 0, \tag{12}$$

where $\tilde{\sigma}_{v_e k}$ and σ_k^* are the relaxed element von Mises stress and stress limit for loading case k, respectively. The maximum function is not differentiable, and since we wish to employ efficient gradient-based techniques for the optimization, we replace the rectifier with a differentiable approximation. Here, we employ the *softplus* function given by

$$x^{+}(x;\kappa) := c + \frac{1}{\kappa} \log \left(e^{\kappa(x-c)} + e^{-\kappa c} \right), \tag{13}$$

where $c = \max(x, 0)$ is used to prevent numerical overflow and κ is a parameter with $\lim_{\kappa \to \infty} x^+(x) = \max(0, x)$. It should be noted that the softplus function is the Kreisselmeier–Steinhauser approximation (Kreisselmeier and Steinhauser 1980) applied to the maximum between zero and x.

As shown in Fig. 1 (solid line), the softplus function attains a small but positive value at x = 0. Therefore, using (13) to replace the rectifier in (12) will indicate the



constraint is violated for stress values close to the limit but nevertheless feasible, and the optimization will consequently render a conservative design. To alleviate this, we shift the function to the right. Since the softplus function is never exactly zero, we cannot attain a shifted function \hat{x}^+ such that $\hat{x}^+(x=0)=0$. Instead, we require $\hat{x}^+(x=0)=\epsilon$, with ϵ a small, specified parameter. The corresponding shifted softplus function is given by

$$\hat{x}^{+}(x;\kappa,\epsilon) := c + \frac{1}{\kappa} \log \left(e^{\kappa(x+x_s-c)} + e^{-\kappa c} \right)$$

$$x_s = \frac{1}{\kappa} \log(e^{\kappa\epsilon} - 1),$$
(14)

with x_s the horizontal shift. The corresponding function is shown with a dashed line in Fig. 1.

With the shifted softplus function, we replace the element constraint of (12) with

$$h(\tilde{\sigma}_{v_e k}) := \hat{x}^+ \left(\frac{\tilde{\sigma}_{v_e k}}{\sigma_k^*} - 1; \kappa, \epsilon \right) \le 0.$$
 (15)

2.3 Aggregated constraint

As in all aggregation methods, we define a single constraint in the optimization problem corresponding to the maximum element stress violation. The optimization problem reads

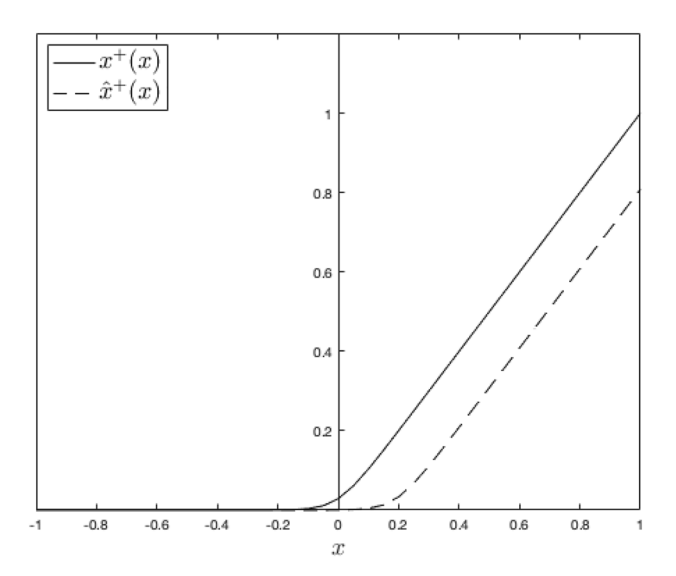


Fig. 1 Softplus smooth rectifier without (solid line) and with (dashed line) shifting. $\kappa=24$ and $\epsilon=0.01$

$$\min_{\rho} v_f := \frac{\sum_{e}^{n_e} \bar{\rho}_e v_e}{\sum_{e}^{n_e} v_e}$$
 (16)

subject to

$$g := \widetilde{\max}_{e,k}(h(\tilde{\sigma}_{v,k}))) \le 0 \tag{17}$$

$$\mathbf{K}\mathbf{u}_k = \mathbf{f}_k, k = 1, \dots, n_k \tag{18}$$

$$\rho_{\min}^2 \le \rho_{\rm e} \le 1, \ i = 1, \dots, n_{\rm e}.$$
(19)

In the expressions above, v_e denotes the element volume and (18) corresponds to the systems of linear equations arising from the finite element discretization of the elasticity boundary value problems for n_k loading cases, with **K** the global stiffness matrix and \mathbf{f}_k the global force vector for loading case k. We assume \mathbf{f}_k to be design independent and the displacement boundary conditions to be the same for all loading cases. In (17), $\widetilde{\text{max}}$ is a differentiable approximation of the maximum function, which in this work we take to be the lower-bound Kreisselmeier-Steinhauser function

$$LKS(\mathbf{x};\beta) := C + \frac{1}{\beta} \log \left(\frac{1}{n} \sum_{i} e^{\beta(x_i - C)} \right), \tag{20}$$

where $C = \max_i x_i$ is used to prevent numerical overflow, n is the number of components of \mathbf{x} , and β is a parameter with $\lim_{\beta \to \infty} LKS(\mathbf{x};\beta) = \max_i x_i$. Note that the maximum in (17) is computed over all elements and all loading cases, hence the vector passed to (20), which following (15) we henceforth denote as \mathbf{h} has $n_e n_k$ components. The rationale for the lower bound on ρ_e in (19) is explained in Sect. 2.5.

One challenge in using the *LKS* function of (20) to compute the maximum stress violation is that this function (as is the case with other aggregation functions) performs poorly when the maximum is close to zero. For this reason, it is undesirable to use a value of ϵ in (14) that is too close to zero. We employ two strategies to circumvent this difficulty. First, we replace $h(\tilde{\sigma}_{v,k})$ with

$$\phi(\tilde{\sigma}_{v_e k}) := e^{h(\tilde{\sigma}_{v_e k})},\tag{21}$$

which for a design with no element stress constraint violations renders a maximum of $e^{\epsilon} \approx 1$. Correspondingly, we replace the constraint (17) with

$$g := LKS(\phi; \beta) - 1 \le 0, \tag{22}$$

where ϕ is the vector of exponentially scaled element stress constraint violations.

The second strategy to address the challenge of approximating the maximum of small numbers is of course to increase the parameter β . However, as noted before, using



286 Page 6 of 17 J. A. Norato et al.

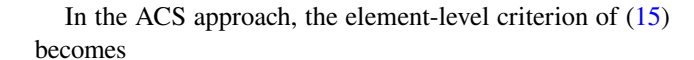
too high a value of β increases the nonlinearity of the constraint and the optimization may converge to a poor local minimum or diverge. To be able to attain a high value of β , we employ a continuation strategy. The optimization starts with a relatively low aggregation parameter β_{\min} until $\max_{e,k} \tilde{\sigma}_{v_e k} < 2\sigma_k^*$ for every loading case k. Thereafter, β is increased at each optimization iteration by an amount $\Delta\beta$ until it reaches a specified value β_{\max} .

The parameter κ in the rectifier function of (15) should also be sufficiently high to accurately approximate the stress constraint violation, and it also increases the nonlinearity of the constraint. Our numerical experiments show that a ratio of $\kappa/\beta=2$ produces good results. Therefore, we also perform continuation on the rectifier parameter κ while maintaining this ratio.

We note that we performed numerical experiments with different combinations of candidate functions for the rectifier of (12) and the aggregation of (17). For instance, we considered the swish function (which is the softmax function applied to the maximum of a number and zero), a smooth Heaviside function, and the (non-differentiable) exponential linear unit (ELU) function for the rectifier approximation. For the aggregate function, we experimented with the P-norm, P-mean, upper-bound KS, softmax, and average functions. Although there may certainly be combinations of different forms for these functions that work as well or better than the ones presented in this work, we obtained the best results (i.e., faster convergence and robustness) with the presented choices, namely the shifted softplus function for the rectifier and the LKS function for the aggregation. The KS function works well for smaller mesh sizes, but the LKS function performs better over the range of mesh sizes presented in the examples. For combinations of the aggregation and rectifier functions that were not effective, the optimization tends to converge to suboptimal designs or get stuck in designs with large gray regions. It is unclear to the authors why this is the case, and an investigation into this aspect is deferred to future work. It is worth noting that different aggregation functions exhibit different asymptotic behaviors; the reader is referred to Verbart (2015) and Kennedy and Hicken (2015) for more details.

2.4 Adaptive constraint scaling

As noted in Sect. 1, we compare the proposed MRF method to the ACS approach of Le et al. (2010). We do not use the regional stress constraints introduced in that work and thus consider a single aggregate-stress constraint. In the following, we briefly describe the ACS method for completeness. For convenience in the derivation and computer implementation, we employ the same notation used to describe our method, which allows us to have a unified sensitivity analysis for both techniques.



$$h(\tilde{\sigma}_{v_e k}) := \frac{\tilde{\sigma}_{v_e k}}{\sigma_k^*},\tag{23}$$

and the aggregate function of (17) becomes

$$g := \gamma \widetilde{\max}_{e,k}(\mathbf{h}) - 1 \le 0. \tag{24}$$

A *P*-norm is used for the differentiable approximation max, given by

$$\|\mathbf{x}\|_{P} := \left[\sum_{i} x_{i}^{P}\right]^{\frac{1}{p}}.$$
(25)

As in our method, the maximum is taken over all elements and all loading cases. The renormalization takes place through the factor γ in (24), which is updated at each iteration I as

$$\gamma^{(I)} = \alpha^{(I)} \frac{\max_{e,k} \left(\tilde{\sigma}_{v_e k}^{(I)} / \sigma_k^* \right)}{\|\mathbf{h}^{(I)}\|_P} + \left(1 - \alpha^{(I)} \right) \gamma^{(I-1)}, \tag{26}$$

where the parameter

$$\alpha^{(I)} = \begin{cases} \alpha_{\text{osc}} & \text{if } I > 3 \text{ and} \\ & (\gamma^{(I-3)} - \gamma^{(I-2)})(\gamma^{(I-2)} - \gamma^{(I-1)}) \\ & < 0 \\ 1.0 & \text{otherwise} \end{cases}$$
 (27)

is used to control fast oscillations of the renormalization. The parameter γ is ignored in the sensitivity analysis (i.e., the sensitivities of g are computed with $\gamma = 1$).

Although the work of Le et al. (2010) uses standard SIMP for material interpolation, here we employ the modified SIMP model of (3) for consistency, as there is no appreciable difference when using either scheme with ACS. The definition of the relaxed stress of (10) is the same.

2.5 Sensitivity analysis

Design sensitivities of the aggregate functions of (17) and (24) can be readily obtained using adjoint differentiation. A detailed derivation is not presented here for brevity, and we only provide the resulting expressions. The sensitivity of g with respect to the filtered density $\bar{\rho}_i$ is given by

$$\frac{\partial g}{\partial \bar{\rho}_i} = \sum_{k=1}^{n_k} \left[\frac{\partial g}{\partial \phi_{i_k}} \frac{\partial \phi_{i_k}}{\partial h_{i_k}} \frac{\partial h_{i_k}}{\partial \bar{\sigma}_{v_i k}} \frac{\partial \tilde{\rho}_i}{\partial \bar{\rho}_i} s_{i_k} + \lambda_k^{\mathrm{T}} \frac{\partial \mathbf{K}}{\partial \bar{\rho}_i} \mathbf{u}_k \right], \tag{28}$$

where λ_k are the solutions to the n_k adjoint problems



In the above expression, \mathbf{L}_e denotes the gather matrix for element e, i.e., the matrix of zeros and ones that maps the global solution vector to the element solution vector (cf. Fish and Belytschko 2007). Conversely, \mathbf{L}_e^T denotes the scatter matrix for element e that maps the element components to the appropriate places in the global vector. These matrices encode the FE assembly process in the equations in terms of matrix multiplications and sum over elements, but are never assembled or stored in the computer code. The terms σ_{e_0k} and s_{e_k} in (29) correspond to (9) and (8) computed for loading case k, respectively. The last term in (28) is obtained from (2) and (3) as

$$\lambda_{k}^{T} \frac{\partial \mathbf{K}}{\partial \bar{\rho}_{i}} \mathbf{u}_{k} = \lambda_{k}^{T} \mathbf{L}_{i}^{T} \frac{\partial \mathbf{K}_{i}}{\partial \bar{\rho}_{i}} \mathbf{L}_{i} \mathbf{u}_{k}$$

$$= \lambda_{ek}^{T} \frac{\partial \mathbf{K}_{i}}{\partial \bar{\rho}_{i}} \mathbf{u}_{ek}$$

$$= p(1 - \rho_{\min}) \bar{\rho}_{i}^{p-1} \lambda_{ek}^{T} \mathbf{K}_{i_{0}} \mathbf{u}_{ek},$$
(30)

where \mathbf{K}_i and \mathbf{K}_{i_0} denote the stiffness matrices for element i computed with the ersatz material of (2) and with \mathbb{C}_0 , respectively, and λ_{ek} and \mathbf{u}_{ek} denote the element adjoint and solution vectors, respectively. From (11), we have

$$\frac{\partial \tilde{\rho}_i}{\partial \bar{\rho}_i} = (p - q)\bar{\rho}_i^{p - q - 1}.$$
(31)

An important point must be made regarding this expression. Since p-q-1<0, as noted in Sect. 2.1, $\partial \tilde{\rho}_i/\partial \bar{\rho}_i$ will be undefined if $\bar{\rho}_i=0$. This means that, unfortunately, we cannot accommodate ρ_e being exactly zero. However, we can impose a lower bound on the design variables that is still much smaller than ρ_{\min} so that the relaxed stress becomes very close to zero as $\bar{\rho}_i \rightarrow 0$. Here, we choose the lower bound to be ρ_{\min}^2 .

The sensitivities of g with respect to the design variables follow from (1) as

$$\frac{\partial g}{\partial \rho} = \mathbf{H} \frac{\partial g}{\partial \bar{\rho}}.\tag{32}$$

The above expressions apply to both the ACS and MRF approaches. For the proposed MRF approach, we have from (15) that

$$\frac{\partial h_{e_k}}{\partial \tilde{\sigma}_{v,k}} = \frac{\partial \hat{\chi}^+}{\partial x} \left(\frac{\tilde{\sigma}_{v_e k}}{\sigma_k^*} - 1; \kappa, \epsilon \right), \tag{33}$$

with

$$\frac{\partial \hat{x}^{+}}{\partial x}(x;\kappa,\epsilon) = \frac{e^{\kappa(x+x_{s}-c)}}{e^{-c\kappa} + e^{\kappa(x+x_{s}-c)}}$$
(34)

from (14). This form can be mathematically simplified, but since the terms have already been computed in (14), this expression reduces additional calculations while preserving the overflow protection. From (21), we have

$$\frac{\partial \phi_{e_k}}{\partial h_{e_k}} = e^{h_{e_k}}. (35)$$

We also have from (22) that

$$\frac{\partial g}{\partial h_{e_k}} = \frac{\partial LKS}{\partial x_i}(\mathbf{x}; \boldsymbol{\beta})|_{x_i \equiv \phi_{e_k}},\tag{36}$$

with

$$\frac{\partial LKS}{\partial x_i}(\mathbf{x}; \boldsymbol{\beta}) = \frac{e^{\beta(x_i - C)}}{\sum_j e^{\beta(x_j - C)}}$$
(37)

from (20).

For the ACS approach, we let $\phi_{e_k} = h_{e_k}$ and therefore $\partial \phi_{e_k}/\partial h_{e_k} = 1$. It follows from (23) that

$$\frac{\partial h_{e_k}}{\partial \tilde{\sigma}_{v_e k}} = \frac{1}{\sigma_k^*},\tag{38}$$

and for the aggregate constraint we find from (24) and (25) that

$$\frac{\partial g}{\partial h_{e_k}} = \left(\frac{h_{e_k}}{g(\mathbf{h})}\right)^{P-1}.$$
(39)

These sensitivities have been verified with finite difference checks for both approaches.

3 Examples

The MRF and ACS methods are implemented in MAT-LAB, version R2022a. For the optimization, we employ the method of moving asymptotes (MMA) (Svanberg 1987, 1998, 2007). We employ the 1999 MATLAB implementation by K. Svanberg, as we found this version significantly outperforms the more widely used 2007 version for both approaches. Both versions exhibit a similar convergence behavior in the first iterations; however, when some solid load paths have been formed but large regions of intermediate density material remain, the 2007 version struggles to continue changing toward a 0–1 design, while the 1999 version makes steady progress in removing gray regions. We posit this may be due to the portions of the MMA formulation that ensure a globally convergent behavior, which



constitute the most significant difference between the two versions; an investigation of this issue, however, is outside the scope of this paper.

To dampen the design steps so as to prevent design changes that may lead to divergence or early convergence to poor minima, we impose a tight move limit m on the design variables and replace (19) with

$$\max(\rho_{\min}^2, \rho_e^{(l-1)} - m) \le \rho_e^{(l)} \le \min(1, \rho_e^{(l-1)} + m). \tag{40}$$

A tighter move limit is required for the MRF approach due to the relatively high values of the aggregation parameter β_{max} . Once the optimization has reached a design for which $\max_{e,k} \tilde{\sigma}_{v_e k} < 1.2\sigma_k^*$ for every loading case k, we double the move limit m to speed up convergence.

To produce a more conservative approximation of the stress constraint in the first iterations of MMA, and in the spirit of Guest et al. (2011), we modify the definition of the asymptotes in the first two iterations of MMA in the MRF approach. The lower and upper asymptotes on design variable x_i are defined as

$$L_i^{(k)} = x_i^{(k)} - s_0(\bar{x}_j - \underline{x}_j) \tag{41}$$

$$U_i^{(k)} = x_i^{(k)} + s_0(\overline{x}_i - \underline{x}_i), \tag{42}$$

respectively, where $k \in \{1, 2\}$ is the iteration number and \underline{x}_j and \overline{x}_j denote the lower and upper bounds on x_j , respectively. The default value of s_0 in MMA is 0.5. Here, we set a much tighter value of $s_0 = m$. The definitions of the asymptotes in the third iteration and thereafter remain unchanged.

The optimization is stopped when the relative change in the objective function in two consecutive iterations is less than $\Delta V_{\rm tol}$ or when $I_{\rm max}$ iterations are reached. Since the tight move limits may occasionally cause premature satisfaction of the former criterion, it is also required that the optimization continues running as long as the gray region fraction G, defined as

$$G := \frac{4}{n_{\rm e}} \sum_{e=1}^{n_{\rm e}} \rho_{\rm e} (1 - \rho_{\rm e}), \tag{43}$$

exceeds a specified value G_{\max} . Unless otherwise noted, the parameter values used in the examples are shown in Table 1.

2D and 3D examples are meshed with bilinear quadrilaterals and trilinear hexahedrals, respectively. Unless otherwise noted, the Young's modulus and Poisson's ratio of the fully-solid material used for all examples are E=1 and $\nu=0.3$, respectively. The 2D examples are solved under plane-stress assumptions. For the 2D problems, the analysis is solved using Cholesky factorization and the Cholesky factor is stored so that the solution of the problems of (29)

Table 1 Parameter values, note h_e is the element size, unless otherwise specified, these are the values used in all examples

Parameter	Value	Reference	
r	$2.5h_{\rm e}$	$2.5h_{\rm e}$ (1)	
p	3	(3)	
$ ho_{ m min}$	10^{-3}	(3)	
q	2.5	(11)	
κ	2β	(14)	
ϵ	10^{-3}	(14)	
β_{\min}	6	Section 2.3	
Δeta	0.2	Section 2.3	
β_{\max}	16	Section 2.3	
P	10	(25)	
$\alpha_{ m osc}$	0.8	(27)	
m	0.02	(40)	
$ ho_{ m e}^{(0)}$	0.5	(40)	
a_0	1	$MMA^{(a)}$	
a_1	0	MMA ^(a)	
c_1	1000	MMA ^(a)	
d_1	1	MMA ^(a)	
$\Delta V_{ m tol}$	10^{-5}	Section 3	
$I_{\rm max}$	500	Section 3	
G_{\max}	0.1	Section 3	

^aSvanberg (1998)

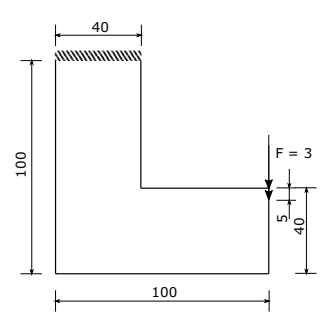


Fig. 2 L-bracket dimensions, load, and boundary conditions

only requires a backward substitution. For the 3D example, we use a preconditioned conjugate gradient method with an incomplete Cholesky factorization for the preconditioner, with a convergence tolerance on the residual of 10⁻⁸. In this case, a full solution must be performed for the primal analysis and for each of the adjoint analyses.

3.1 L-bracket

The first example we present is the L-bracket, widely used as a benchmark in stress-constrained topology optimization (see, for example, Duysinx and Bendsøe (1998)). The purpose of this example is to compare the performance of the MRF and ACS approaches for varying aggregation parameter values. The dimensions, loading, and boundary



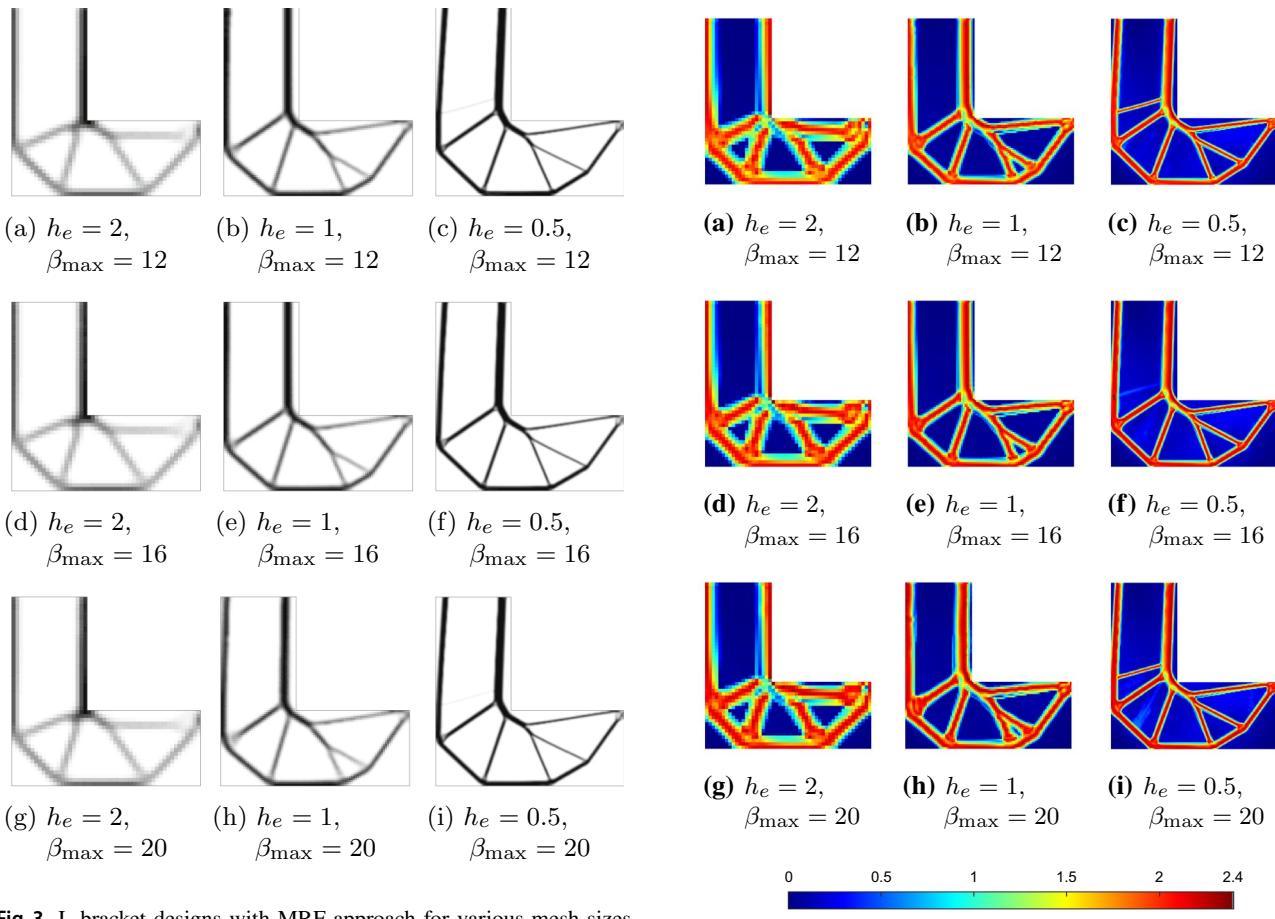


Fig. 3 L-bracket designs with MRF approach for various mesh sizes and aggregation parameters $\beta_{\rm max}$

Fig. 4 Relaxed stress $\tilde{\sigma}_{\nu}$ for the MRF L-bracket designs of Fig. 3

conditions are shown in Fig. 2. The load is distributed over a short length to avoid a stress concentration at its point of application. The L-bracket is meshed with element sizes $h_{\rm e}=2$ (1,600 elements), $h_{\rm e}=1$ (6,400 elements), and $h_{\rm e}=0.5$ (25,600 elements). The stress limit for this problem is $\sigma_1^*=2.4$.

The designs obtained for this problem are shown in Fig. 3 for the MRF approach with three values of the maximum aggregation parameter β_{max} and in Fig. 7 for the ACS method with three values of the aggregation parameter P. In both cases, the second and third aggregation parameter values correspond to a 1/3 and 2/3 increase of the lower value, respectively ($\beta_{\text{max}} = 12, 16, 20$ for the MRF approach and P = 6, 8, 10 for the ACS approach). Figures 4 and 8 show the relaxed stresses; Figs. 5 and 9 show the objective function history; and Figs. 6 and 10 show the logarithm of the true maximum stress history for the two approaches. Values of the volume fraction, true maximum stress, and number of iterations to convergence for these two sets of runs are listed in Table 2.

Several observations can be made from these results. The most important difference between the two methods is the robustness of the proposed MRF approach with respect to changes in the aggregation parameter. The MRF designs of Fig. 3 are similar for the same element

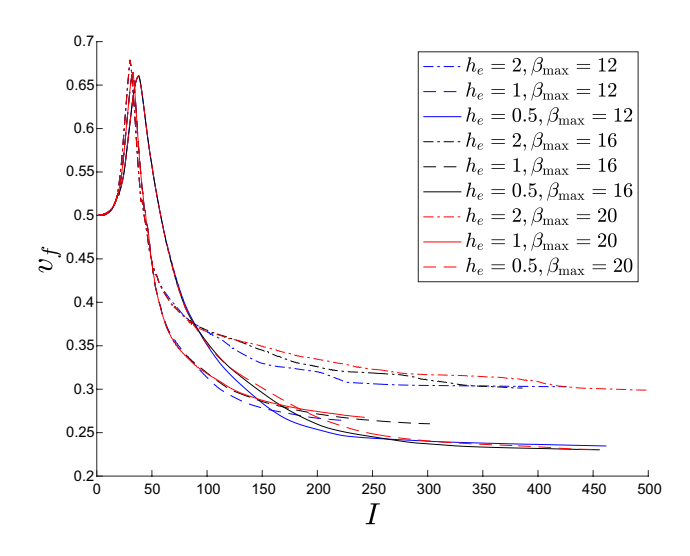


Fig. 5 Objective function history for the MRF designs of Fig. 3



286 Page 10 of 17 J. A. Norato et al.

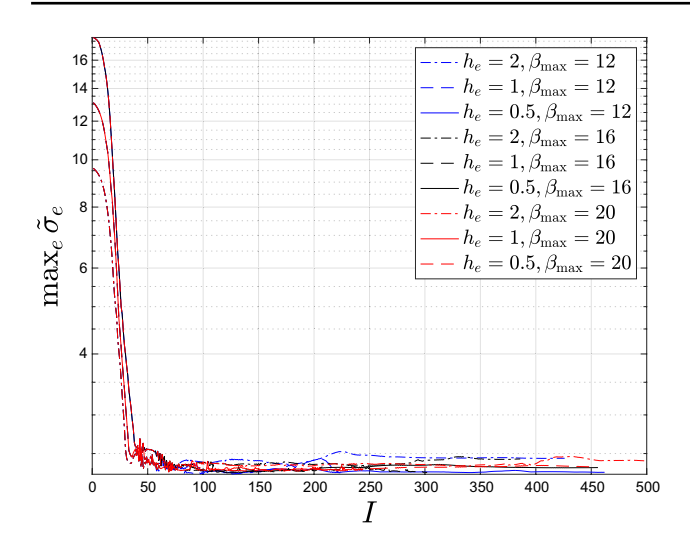


Fig. 6 True maximum stress history for the MRF designs of Fig. 3

size, whereas those of the ACS approach shown in Fig. 7 are highly dependent on the value of the aggregation parameter. A small change in *P* leads to significantly

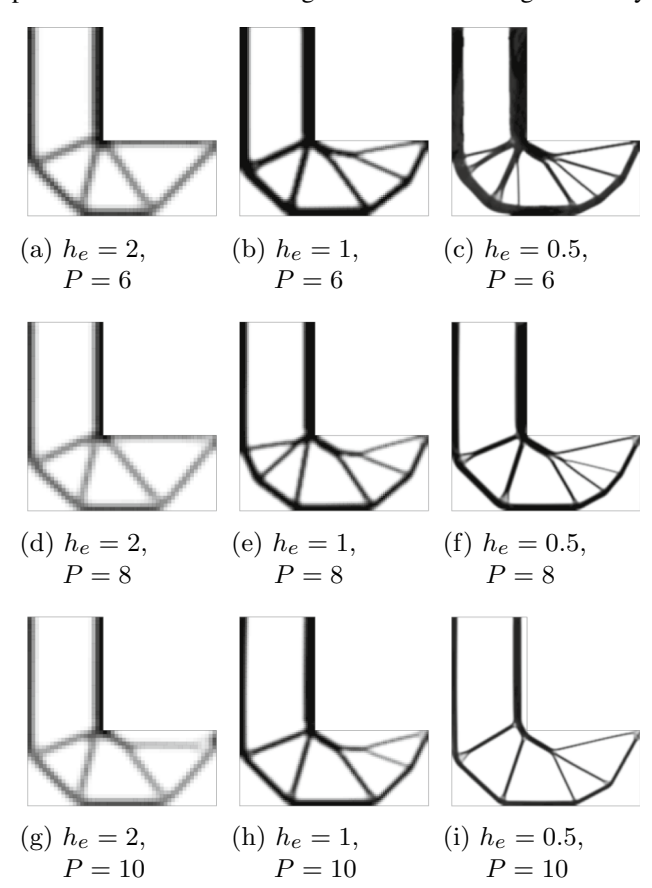


Fig. 7 L-bracket designs with ACS approach for various mesh sizes and aggregation parameters

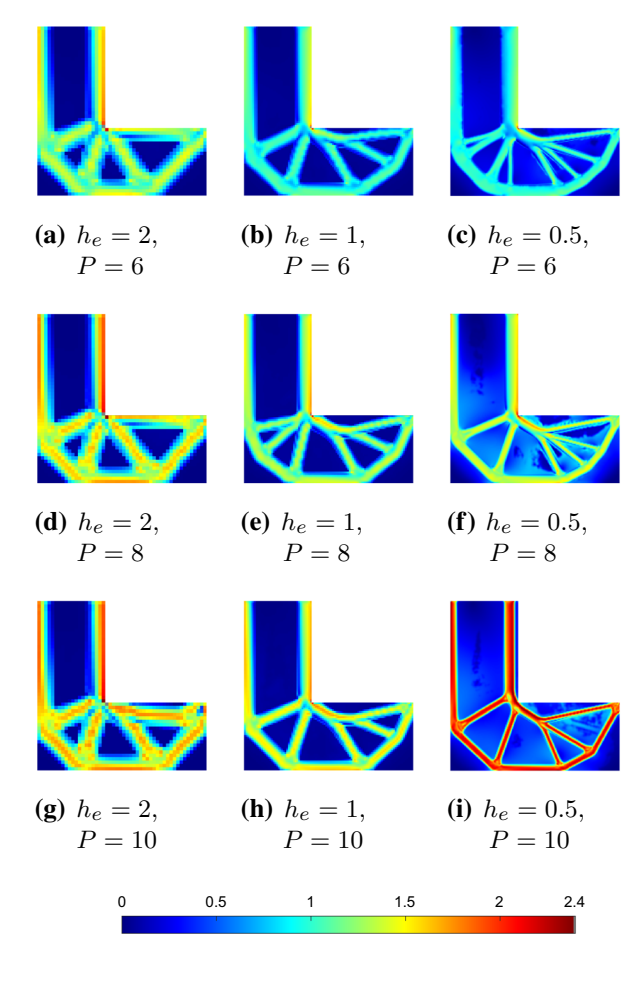
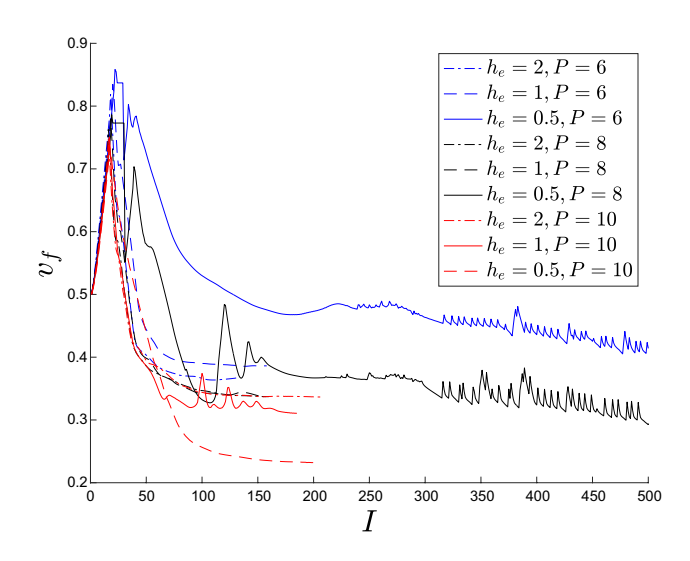


Fig. 8 Relaxed stress $\tilde{\sigma}_{v_a}$ for the ACS L-bracket designs of Fig. 7



 $\textbf{Fig. 9} \ \ \textbf{Objective function history for the ACS designs of Fig. 7}$



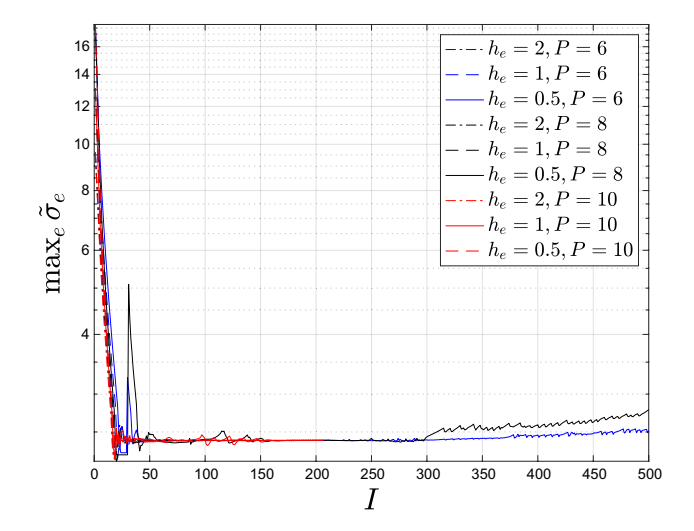


Fig. 10 True maximum stress history for the ACS designs of Fig. 7

different results, in some cases leading to suboptimal designs (e.g., the design for $h_{\rm e}=0.5$, P=6), inability to remove the stress concentration around the re-entrant corner ($h_{\rm e}=2$, P=6), or occasionally divergence. It is likely that the continuation approach in the MRF method steers the optimization toward the same local minimum, but that is arguably an advantage, particularly given that

the volume fraction of the MRF designs is comparable (or in several cases substantially better) than that obtained with the ACS technique.

Another stark evidence of the robustness of the proposed approach is its convergence behavior. As seen in 5, the objective function decreases smoothly, whereas the ACS approach (Fig. 9) exhibits a more oscillatory behavior. This behavior is purely a byproduct of the renormalization, and it not only hinders convergence, but in some cases can lead to a poor local minimum after having reached a better minimum, as in the design obtained for $h_{\rm e}=0.5$ and P=6 (Fig. 8). To be sure, the ACS approach can obtain good designs, but its success depends on the choice of the aggregation parameter P. Unfortunately, there is no clear guideline as to how to choose a good value of P a priori, thus requiring trial and error.

To examine how well the aggregation function scales with the number of elements, we repeat the optimization of the L-bracket with the MRF approach using three larger meshes, see Fig. 11 and Table 2. All runs are performed with $\beta_{\text{max}} = 16$. As the number of elements increases, convergence becomes slower and so for these runs we use a larger move limit (m = 0.04) and filter radius than in the previous runs. We also impose $I_{\text{max}} = 1,000$.

These runs show that the optimizer is able to satisfy relatively well the stress constraint with the same aggregation

Table 2 Values for the designs of Figs. 3 and 7

	h_{e}	β/P	v_f	$\sigma_{ m max}$	$\Delta\sigma_{\max}\left(\%\right)$	It.	Figure
MRF	2	$\beta = 12$	0.303	2.445	1.87	425	3a
	2	$\beta = 16$	0.301	2.437	1.53	385	3d
	2	$\beta = 20$	0.299	2.414	0.59	500	3 g
	1	$\beta = 12$	0.264	2.284	-4.82	223	3 b
	1	$\beta = 16$	0.260	2.290	- 4.57	301	<u>3</u> e
	1	$\beta = 20$	0.268	2.327	-3.03	242	3h
	0.5	$\beta = 12$	0.235	2.288	- 4.66	461	3c
	0.5	$\beta = 16$	0.230	2.340	- 2.51	455	3f
	0.5	$\beta = 20$	0.231	2.348	- 2.15	449	3i
	0.25	$\beta = 16$	0.228	2.363	- 1.54	446	11a
	0.20	$\beta = 16$	0.244	2.341	- 2.47	483	11b
	0.16	$\beta = 16$	0.307	2.376	- 1.02	1000	11c
ACS	2	P = 6	0.368	2.399	- 0.03	133	7 a
	2	P = 8	0.337	2.400	0.01	159	7 d
	2	P = 10	0.337	2.400	- 0.01	206	7 g
	1	P = 6	0.386	2.400	- 0.01	157	7 b
	1	P = 8	0.338	2.402	0.07	155	7 e
	1	P = 10	0.311	2.399	- 0.03	184	7 h
	0.5	P = 6	0.409	2.523	5.11	500	7 c
	0.5	P = 8	0.321	2.753	14.70	500	7 f
	0.5	P = 10	0.232	2.399	-0.02	199	7 i

 σ_{\max} denotes the true largest stress and $\Delta\sigma_{\max}$ is its value relative to the stress limit σ_1^* . It is the number of iterations to satisfy at least one of the stopping criteria



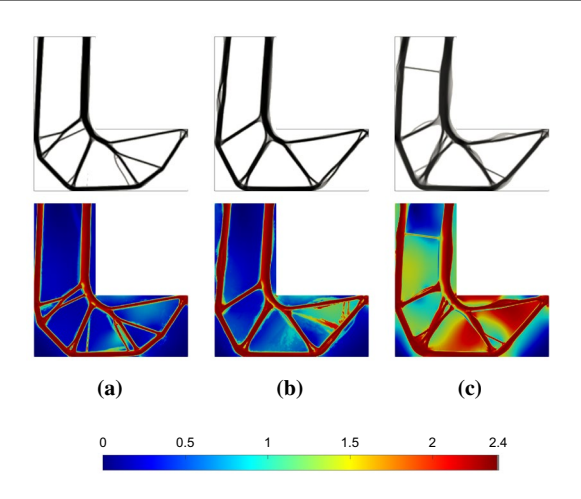


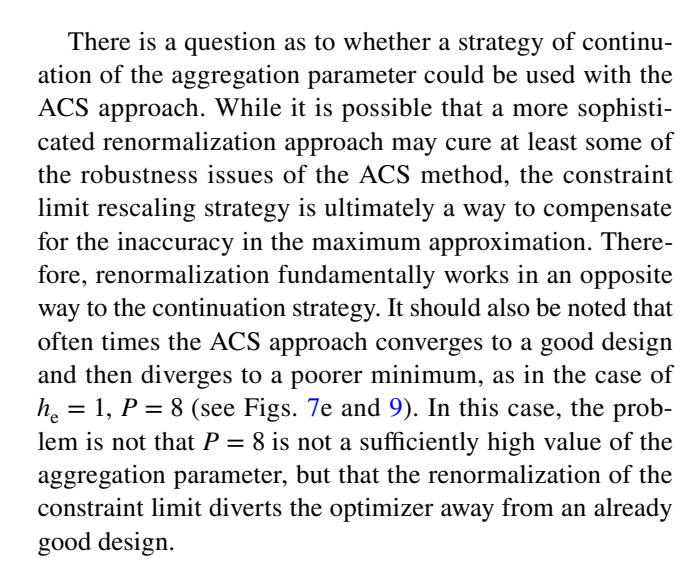
Fig. 11 L-bracket designs with MRF approach for larger mesh sizes. **a** $h_{\rm e}=0.25$ (102,400 elements) with $r=3h_{\rm e}$. **b** $h_{\rm e}=0.20$ (160,000 elements) with $r=3h_{\rm e}$. **c** $h_{\rm e}=0.16$ (250,000 elements), with $r=4h_{\rm e}$

parameter values used before, hence the aggregation scales well in this sense. However, with decreasing element size, the optimizer is unable to efficiently remove gray regions after some point, even though the design is reasonable (i.e., similar to the ones obtained with coarser meshes). This behavior does not improve by decreasing or increasing β_{max} . Moreover, as observed in Fig. 11, there are increasingly larger gray regions with active stress constraints as the element size decreases. Therefore, this behavior is more likely due to the relaxation. A further investigation of this issue is deferred to future work.

Despite the fact that the proposed approach is able to reasonably satisfy the stress constraints across the mesh sizes used in this example, we make no claim that the effectiveness of the proposed MRF method is completely insensitive to the aggregation parameter β . It is clear from these examples, however, that it is a more robust method than the ACS approach.

It can also be observed that the MRF approach produces more fully-stressed designs than the ACS method, as seen in Figs. 4 and 8. As noted in Sect. 2.5, the sensitivities in the ACS approach are inconsistent as they cannot capture changes in the scaling parameter γ of (26). This inconsistency may prevent the optimizer from getting closer to a fully stressed design in some cases.

Finally, it should be noted that, in general and as expected, the ACS approach is able to more tightly satisfy the stress constraint, as seen in Table 2. However, as seen in the table, the ACS approach can occasionally end up violating the constraint significantly, as is the case for h = 0.5 and P = 8. The MRF designs are all reasonably close to the limit in all cases. Also, all the MRF designs are lighter than those obtained with the ACS approach.



3.2 Portal frame

The next example corresponds to the portal frame design presented in Le et al. (2010). The dimensions, loading, and boundary conditions are shown in Fig. 12a. In Le et al. (2010), the optimization minimizes the maximum stress subject to a volume fraction constraint of 0.3, rendering a design with $\sigma_{\rm max}=3.3$. Here, we solve the volume fraction minimization problem of (16)–(19) with $\sigma_1^*=3.3$. A uniform mesh of 240×80 elements is deformed vertically to create the V-shaped cutout and horizontally to maintain a good aspect ratio.

Figure 12b and c shows the results of the optimization using the MRF and ACS methods, respectively. For comparison, the minimum-compliance design is shown in Fig. 12d, with a constraint that the volume fraction does not exceed that of the optimal MRF design of Fig. 12c. This result is obtained with a scaling factor of 0.01 for the structural compliance C and with m = 0.1. For this example, both MRF and ACS approaches produce a similar design. Interestingly, they both render much lighter designs than the one reported in Le et al. (2010), which is possibly due to the smaller element size used here.

3.3 Cracked design region

The following example consists of the cracked design region presented in Emmendoerfer Jr and Fancello (2014). We employ the modified version shown in Giraldo-Londoño and Paulino (2021), with the Mode-I loading shown in Fig. 13a. Symmetry boundary conditions are imposed to model only half of the design region, with a mesh of 100×200 elements. The Young's modulus and Poisson's ratio for this example are E=70 GPa and v=0.25, respectively. The stress limit is $\sigma_1^*=100$ MPa. For the ACS method, it is necessary to use a higher value of the aggregation parameter to obtain a design



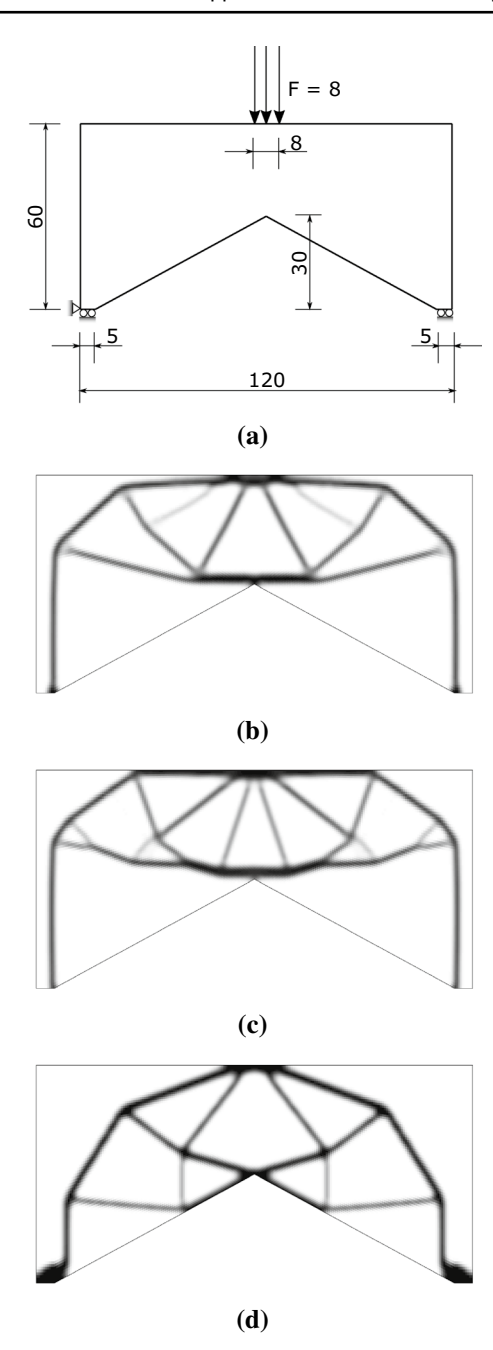


Fig. 12 Portal frame design. **a** Dimensions, loading, and boundary conditions. **b** MRF design with $v_f = 0.213$, $\sigma_{\rm max} = 3.311$, $\Delta\sigma_{\rm max} = 0.33\%$, It. = 361, and $C = 5.86{\rm E3}$. **c** ACS design with $v_f = 0.224$, $\sigma_{\rm max} = 3.298$, $\Delta\sigma_{\rm max} = -0.07\%$, It. = 316, and $C = 5.75{\rm E3}$. **d** Minimum-compliance design with $v_f = 0.213$, $\sigma_{\rm max} = 9.076$, $\Delta\sigma_{\rm max} = 175.02\%$, It. = 92, and $C = 4.23{\rm E3}$

similar in volume fraction to the one produced by the MRF approach; after some trial and error, we found P = 16 to be an adequate value.

The designs obtained with the MRF and ACS methods are shown in Fig. 13b and c, respectively. For this problem, the MRF method produces a lighter design than the ACS

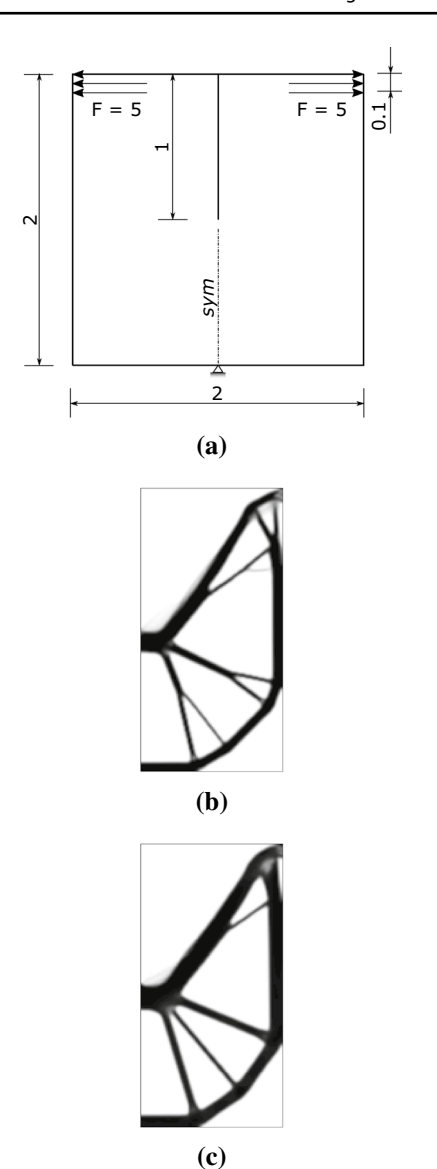


Fig. 13 Cracked plate design. **a** Dimensions (in m), loading (in kN), and boundary conditions. **b** MRF design with $v_f = 0.267$, $\sigma_{\text{max}} = 101.316$, $\Delta \sigma_{\text{max}} = 1.32\%$, and It. = 442. **c** ACS design with $v_f = 0.321$, $\sigma_{\text{max}} = 100.107$, $\Delta \sigma_{\text{max}} = 0.11\%$, and It. = 281

approach. It is also interesting to note in this example that the MRF design shows some internal members with forked, Y-shaped ends, which presumably split the load going into the outer member to reduce stresses at the joints.

3.4 Double L-bracket

In this section, we consider the double L-bracket shown in Fig. 14a and introduced in Le et al. (2010). The purpose of this example is to demonstrate the method with multiple load cases. The loading for one load case is a reflection of the loading for the other, but the stress limits are different: $\sigma_1^* = 1.8$ and $\sigma_2^* = 2.4$ for the right-hand and left-hand



286 Page 14 of 17 J. A. Norato et al.

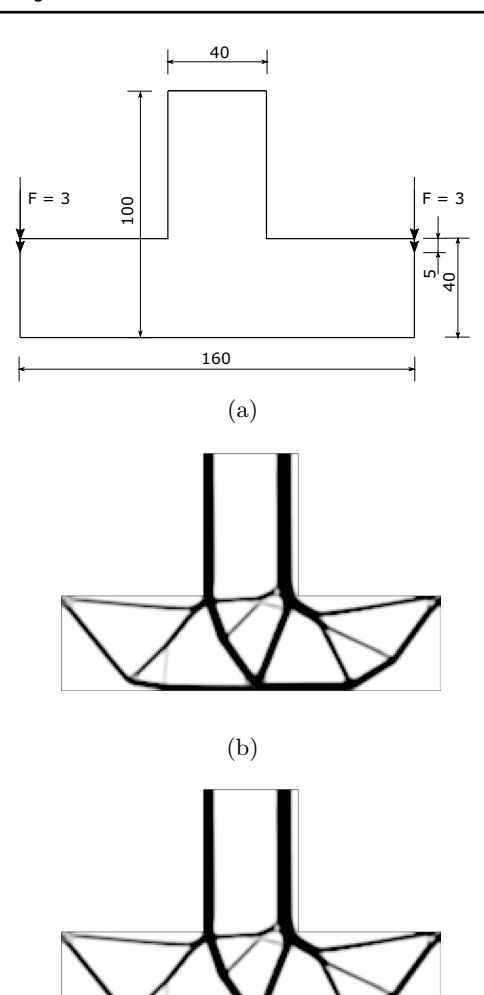


Fig. 14 Double L-bracket design. **a** Dimensions, loading, and boundary conditions. **b** MRF design with $v_f = 0.295$, $\sigma_{1_{\text{max}}} = 1.807$, $\sigma_{2_{\text{max}}} = 2.553$ $\Delta\sigma_{1_{\text{max}}} = 0.41\%$, $\Delta\sigma_{2_{\text{max}}} = 6.36\%$, and It. = 500. **c** ACS design with $v_f = 0.348$, $\sigma_{1_{\text{max}}} = 1.799$, $\sigma_{2_{\text{max}}} = 2.237$ $\Delta\sigma_{1_{\text{max}}} = -0.07\%$, $\Delta\sigma_{2_{\text{max}}} = -6.79\%$, and It. = 244

(c)

loads, respectively. The mesh uses 13,150 uniform elements of size $h_{\rm e}=0.8$. Figure 14b and c shows the designs obtained with the MRF and ACS methods, respectively. We use P=16 for the ACS method, as it produces a better design than P=10.

The MRF and ACS approaches render similarly performing designs for this example; however, the ACS design more tightly satisfies the stress limits. As with the aggregate constraint for multiple load cases introduced in Le et al. (2010), the function (17) in the proposed method is equally effective in incorporating local stress constraints for multiple load cases and different stress limits using a single constraint (although, as discussed in Sect. 2.5, one sensitivity analysis per load case is nevertheless required).

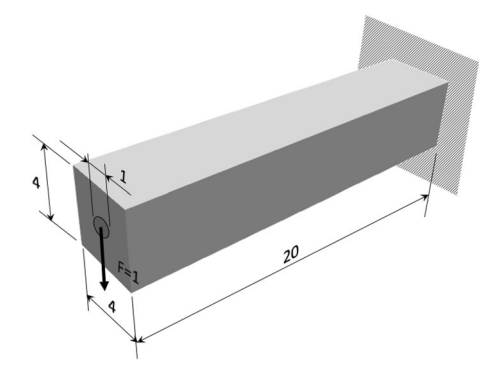


Fig. 15 Dimensions, boundary conditions, and load for the 3D cantilever beam example

3.5 3D cantilever

The last example we present corresponds to the design of the 3D cantilever beam shown in Fig. 15. Symmetry boundary conditions are employed and the half design region is meshed with $160 \times 32 \times 16$ hexahedral elements. The load is distributed uniformly within a circular region centered at the midpoint of the end face. We use a filter radius $r = 2h_{\rm e}$ and a larger stopping criterion of $G_{\rm max} = 0.15$ for the gray region fraction. The stress limit is $\sigma_1^* = 5$.

The solution of the stress-constrained optimization for this problem using the MRF approach with the aggregation parameter value of $\beta_{\text{max}} = 16$ listed in Table 1 renders a design that violates the stress constraint by about 4.7%. To render a tighter constraint satisfaction, we use a higher value of $\beta_{\text{max}} = 32$.

Figure 16 shows the designs obtained with the MRF and ACS approaches. For comparison, the minimum-compliance design with the same volume fraction as that of the MRF design and with a move limit m=0.1 is also shown. The ACS result is obtained using P=20. Looser tolerances $\Delta V_{tol}=5\times 10^{-5}$ and $G_{\rm max}=0.3$ must be used for the ACS method, as no convergence was achieved with the tolerance values of Table 1 and with various values of P. In those cases, the optimizer reaches a volume fraction similar to that of the design shown in Fig. 16 (center) and then it diverges as in other examples. The MRF approach, on the other hand, exhibits smooth convergence and renders a design that is lighter and clearly more fully-stressed than the ACS design, with a reasonably close stress limit satisfaction.

It is also interesting to note for this example that, even though the design region does not have re-entrant corners, there is a stress concentration at the wall due to the aspect ratio of the design region, which prevents the development of a more optimal parabolic outer shape; see, for example, Shin et al. (2015) and Norato (2018). This explains why the stress-constrained designs are so different from the



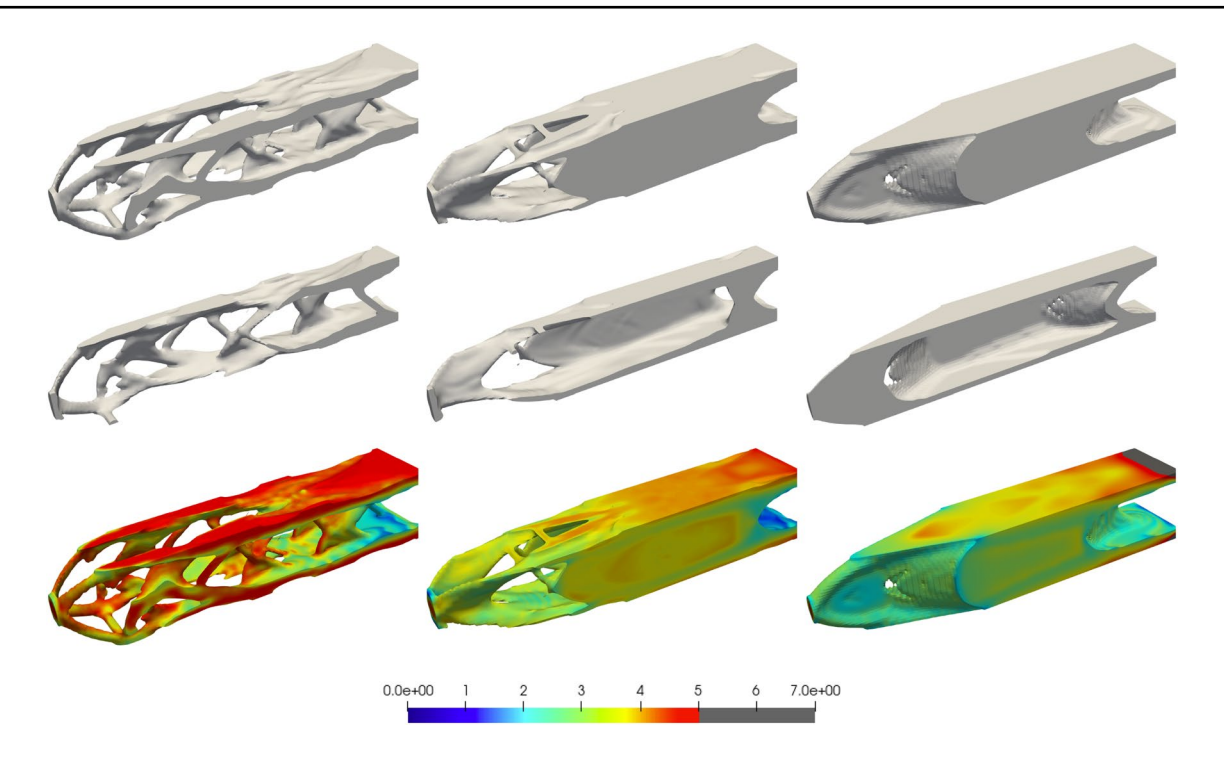


Fig. 16 Stress-constrained designs using MRF (left) and ACS (center) approaches and minimum-compliance design (right) for cantilever beam. Top row shows a density iso-surface of the entire beam, and the middle row shows a cut through the half-plane to reveal internal features. The bottom row shows the corresponding element

stresses. MRF design has $v_f = 0.32$, $\sigma_{\max} = 5.112$, $\Delta \sigma_{\max} = 2.24\%$, It. = 314, and C = 6.89E2. ACS design has $v_f = 0.358$, $\sigma_{\max} = 4.999$, $\Delta \sigma_{\max} = -0.01\%$, It. = 220, and C = 5.34EE2. Minimum-compliance design has $v_f = 0.32$, $\sigma_{\max} = 7.409$, $\Delta \sigma_{\max} = 48.18\%$, It. = 81, and C = 4.87E2

minimum-compliance design, since in the absence of this stress concentration and with a single loading, one would otherwise expect the strongest design to be the same as the stiffest design (cf., Pedersen 2000).

4 Conclusion

This work introduced an aggregation method for stressconstrained, density-based topology optimization that does not require renormalization of the constraint to attain the specified stress limit. The presented examples demonstrate that the proposed method is effective and more robust with respect to the aggregation parameters than the ACS technique. For several of the examples, it was necessary to experiment with different values of the aggregation parameter P in the ACS approach to obtain convergence to a good design. The proposed MRF approach, on the other hand, rendered good results with no variation to the aggregation and rectifier parameters listed in Table 1 (with the exception of the example of Sect. 3.5, in which a higher value of the aggregation parameter was used to obtain a tighter constraint satisfaction). The proposed technique therefore circumvents the need for renormalization while allowing the strength requirements to be imposed as a separate constraint in the optimization problem as in all aggregation techniques.

We reiterate no claim is made that our method is parameter independent. However, the fact that the proposed approach is able to attain good designs with a fixed set of aggregation parameters demonstrates the significant increase in robustness with respect to the renormalization approach. As expected, the proposed method does not satisfy the stress constraint as tightly as the ACS approach; however, the constraint satisfaction is adequate for design practice.

The fact that various strategies must be employed to account for the nonlinearity of the constraint to prevent poor design steps in MMA is an indication that this method could greatly benefit of more robust optimization approaches—for instance, endowing the design step with a line search. This would likely circumvent the need for move limits by enforcing small design steps when the approximation is inaccurate and the design is away from the feasible boundary, and allowing for larger design steps for faster convergence otherwise. As noted in Sect. 3.1, further investigation is needed on the stress relaxation scheme to improve the convergence of the proposed method for large mesh sizes.

There are many possible extensions to this work based on state-of-the-art techniques in stress-constrained topology optimization, such as incorporating a projection filter to



substantially reduce the gray region fraction (e.g., De Troya and Tortorelli 2018) or employing inexact sensitivities to speed up the optimization (cf., Amir 2021). These potential improvements were not explored here, as the goal of this work is to demonstrate that, even without them, the proposed technique effectively and robustly circumvents the need for renormalization.

Finally, we demonstrated our method in the context of density-based topology optimization with stress constraints. However, just as the ACS approach has been used in level-set techniques (cf., Picelli et al. 2018) and in geometry projection methods for topology optimization with geometric primitives (cf., Zhang et al. 2020), we expect the proposed MRF technique to be readily extended to those realms. Likewise, we also expect it to be possible to employ the proposed method in fatigue-based topology optimization techniques for which the ACS method has been used before (e.g., Oest and Lund 2017; Zhang et al. 2019).

Appendix: Robust calculation of σ_{v_a}

It is worth noting that some works [for example, Duysinx and Bendsøe (1998) and Le et al. (2010)] define a matrix $\mathbf{M}_e := \mathbf{B}_e^T \mathbb{C}_0 \mathbf{V} \mathbb{C}_0 \mathbf{B}_e$ for each element that is computed once at the beginning of the optimization and stored, and subsequently compute $s_e = \sqrt{\mathbf{u}_e^T \mathbf{M}_e \mathbf{u}_e}$. The matrix \mathbf{M}_e is positive semidefinite, thus the quadratic form in (8) can be zero. Indeed, s_e must be zero if a non-zero displacement \mathbf{u}_e corresponds to a rigid-body motion that would cause no deformation. Although the displacement boundary conditions prevent a rigid-body motion of the entire structure, some regions can experience rigid-body motion. For example, in a cantilever beam with a bending load applied in between the wall and the free end of the beam, the region of the beam between the load and the free end will experience rigid-body motion regardless of its stiffness.

While the positive semidefiniteness of \mathbf{M}_e should cause no problem in exact arithmetic, it is possible (as we in fact observed in some of our numerical experiments) that a computer calculation of \mathbf{M}_e may have a near-zero but negative eigenvalue, thus the quadratic form in (8) can be negative. Moreover, \mathbf{V} in \mathbb{R}^3 also has a zero eigenvalue; computing numerically the eigenvalues of \mathbf{V} in \mathbb{R}^3 in Matlab using the eig function, for example, renders a near-zero but negative eigenvalue, while a symbolic computation in Mathematica using the Eigenvalues function renders an exactly zero eigenvalue.

Computing s_e using (9) first and then (8) circumvents this problem, since even if **V** has a negative eigenvalue, $\sigma_{e_0} = \mathbf{0}$ for a rigid-body displacement, hence the argument of the square root would be zero. This is therefore a more robust

approach. Furthermore, computing s_e in this manner requires significantly fewer floating point operations (about half for n = 2 and less than a third for n = 3) and storing \mathbf{B}_e requires less memory than storing \mathbf{M}_e (less than half for n = 2 and one-fourth for n = 3), which can be substantial for meshes with non-uniform element shapes, such as the one used in the example of Sect. 3.2.

Acknowledgements This research was supported in part by the Air Force Research Laboratory, Aerospace Systems Directorate, through the Air Force Office of Scientific Research Summer Faculty Fellowship Program®, Contract Numbers FA8750-15-3-6003 and FA9550-15-0001. The first author also gratefully acknowledges partial support to conduct this work from the US National Science Foundation, award CMMI-1751211. We thank Prof. Krister Svanberg for kindly providing his MMA MATLAB optimizer to perform the optimization.

Declarations

Conflict of interest The authors declare they have no conflict of interest.

Replication of results The MATLAB code used to implement the ACS and MRF methods, along with the input files for all the examples shown in this manuscript, are available through GitHub at https://github.com/jnorato/MRF.

References

- Amir O (2021) Efficient stress-constrained topology optimization using inexact design sensitivities. Int J Numer Methods Eng 122(13):3241–3272
- Amstutz S, Novotny AA (2010) Topological optimization of structures subject to von Mises stress constraints. Struct Multidisc Optim 41(3):407–420
- Bendsøe MP, Sigmund O (1999) Material interpolation schemes in topology optimization. Arch Appl Mech 69(9):635–654
- Birgin EG, Castillo RA, Martínez JM (2005) Numerical comparison of augmented Lagrangian algorithms for nonconvex problems. Comput Optim Appl 31(1):31–55
- Bourdin B (2001) Filters in topology optimization. Int J Numer Methods Eng 50(9):2143–2158
- Bruggi M (2008) On an alternative approach to stress constraints relaxation in topology optimization. Struct Multidisc Optim 36(2):125–141
- Bruns TE, Tortorelli DA (2001) Topology optimization of non-linear elastic structures and compliant mechanisms. Comput Methods Appl Mech Eng 190(26–27):3443–3459
- Cheng GD, Guo X (1997) ε-relaxed approach in structural topology optimization. Struct Optim 13(4):258–266
- Cheng G, Jiang Z (1992) Study on topology optimization with stress constraints. Eng Optim 20(2):129–148
- Curtis FE, Gould NI, Jiang H, Robinson DP (2016) Adaptive augmented Lagrangian methods: algorithms and practical numerical experience. Optim Methods Softw 31(1):157–186
- da Silva GA, Aage N, Beck AT, Sigmund O (2021) Local versus global stress constraint strategies in topology optimization: a comparative study. Int J Numer Methods Eng 122(21):6003–6036



- De Troya MAS, Tortorelli DA (2018) Adaptive mesh refinement in stress-constrained topology optimization. Struct Multidisc Optim 58(6):2369–2386
- Duysinx P, Bendsøe MP (1998) Topology optimization of continuum structures with local stress constraints. Int J Numer Methods Eng 43(8):1453–1478
- Emmendoerfer H Jr, Fancello EA (2014) A level set approach for topology optimization with local stress constraints. Int J Numer Methods Eng 99(2):129–156
- Fish J, Belytschko T (2007) A first course in finite elements. Wiley, New York
- Giraldo-Londoño O, Paulino GH (2021) Polystress: a Matlab implementation for local stress-constrained topology optimization using the augmented Lagrangian method. Struct Multidisc Optim 63(4):2065–2097
- Giraldo-Londoño O, Aguiló MA, Paulino GH (2021) Local stress constraints in topology optimization of structures subjected to arbitrary dynamic loads: a stress aggregation-free approach. Struct Multidisc Optim 2021:1–23
- Guest JK, Asadpoure A, Ha SH (2011) Eliminating beta-continuation from Heaviside projection and density filter algorithms. Struct Multidisc Optim 44(4):443–453
- Kennedy GJ, Hicken JE (2015) Improved constraint-aggregation methods. Comput Methods Appl Mech Eng 289:332–354
- Kirsch U (1990) On singular topologies in optimum structural design. Struct Optim 2(3):133–142
- Kreisselmeier G, Steinhauser R (1980) Systematic control design by optimizing a vector performance index. Computer aided design of control systems. Elsevier, New York, pp 113–117
- Le C, Norato J, Bruns T, Ha C, Tortorelli D (2010) Stress-based topology optimization for continua. Struct Multidisc Optim 41(4):605-620
- Norato JA (2018) Topology optimization with supershapes. Struct Multidisc Optim 58(2):415–434
- Oest J, Lund E (2017) Topology optimization with finite-life fatigue constraints. Struct Multidisc Optim 56(5):1045–1059
- Pedersen P (2000) On optimal shapes in materials and structures. Struct Multidisc Optim 19(3):169–182
- Pereira JT, Fancello EA, Barcellos CS (2004) Topology optimization of continuum structures with material failure constraints. Struct Multidisc Optim 26(1–2):50–66
- Picelli R, Townsend S, Brampton C, Norato J, Kim HA (2018) Stressbased shape and topology optimization with the level set method. Comput Methods Appl Mech Eng 329:1–23
- Rozvany G, Birker T (1994) On singular topologies in exact layout optimization. Struct Optim 8(4):228–235
- Rozvany G, Sobieszczanski-Sobieski J (1992) New optimality criteria methods: forcing uniqueness of the adjoint strains by corner-rounding at constraint intersections. Struct Optim 4(3–4):244–246
- Russ JB, Waisman H (2021) A novel elastoplastic topology optimization formulation for enhanced failure resistance via local ductile failure constraints and linear buckling analysis. Comput Methods Appl Mech Eng 373:113478

- Senhora FV, Giraldo-Londono O, Menezes IF, Paulino GH (2020) Topology optimization with local stress constraints: a stress aggregation-free approach. Struct Multidisc Optim 62(4):1639–1668
- Shin M, Tortorelli D, Norato J (2015) Optimal shape design of axisymmetric structures subject to asymmetric loading. Comput Methods Appl Mech Eng 293:283–305
- Sigmund O (2007) Morphology-based black and white filters for topology optimization. Struct Multidisc Optim 33(4–5):401–424
- Svanberg K (1987) The method of moving asymptotes—a new method for structural optimization. Int J Numer Methods Eng 24(2):359–373
- Verbart A, Langelaar M, Van Keulen F (2017) A unified aggregation and relaxation approach for stress-constrained topology optimization. Struct Multidisc Optim 55(2):663–679
- Wang C, Qian X (2018) Heaviside projection-based aggregation in stress-constrained topology optimization. Int J Numer Methods Eng 115(7):849–871
- Yang R, Chen C (1996) Stress-based topology optimization. Struct Optim 12(2):98–105
- Zhang S, Le C, Gain AL, Norato JA (2019) Fatigue-based topology optimization with non-proportional loads. Comput Methods Appl Mech Eng 345:805–825
- Zhang JZ, Sharpe C, Seepersad CC (2020) Stress-constrained design of functionally graded lattice structures with spline-based dimensionality reduction. J Mech Des 142(9):091702
- Zhou M, Sigmund O (2017) On fully stressed design and *p*-norm measures in structural optimization. Struct Multidisc Optim 56(3):731–736
- Duysinx P, Sigmund O (1998) New developments in handling stress constraints in optimal material distribution. In: 7th AIAA/USAF/ NASA/ISSMO symposium on multidisciplinary analysis and optimization, p. 4906
- Svanberg K (1998) The method of moving asymptotes-modelling aspects and solution schemes. In: Lecture notes for the DCAMM course advanced topics in structural optimization. http://www.ingveh.ulg.ac.be/uploads/education/meca-0027-1/MMA_DCAMM_1998.pdf
- Svanberg K (2007) MMA and GCMMA, versions September 2007. In: Optimization and Systems Theory, p 104. https://people.kth.se/~krille/gcmma07.pdf
- Verbart A (2015) Topology optimization with stress constraints. PhD thesis, Delft University of Technology

Publisher's Note Springer Nature remains neutral with regard to jurisdictional claims in published maps and institutional affiliations.

Springer Nature or its licensor holds exclusive rights to this article under a publishing agreement with the author(s) or other rightsholder(s); author self-archiving of the accepted manuscript version of this article is solely governed by the terms of such publishing agreement and applicable law.

